On filtering in the viscous-convective subrange for turbulent mixing of high Schmidt number passive scalars

Siddhartha Verma[1,a)] and G. Blanquart[2,b)]
[1]*Graduate Aerospace Laboratories, California Institute of Technology, Pasadena, California 91125, USA*
[2]*Department of Mechanical Engineering, California Institute of Technology, Pasadena, California 91125, USA*

In the present work, we investigate the possibility of performing velocity-resolved, scalar-filtered (VR-SF) numerical simulations of turbulent mixing of high Schmidt number scalars, by using a Large Eddy Simulation (LES)-type filter in the viscous-convective subrange. The only requirement for this technique is the large scale separation between the Kolmogorov and Batchelor length scales, which is a direct outcome of the high Schmidt number of the scalar. The present *a priori* analysis using high fidelity direct numerical simulation data leads to two main observations. First, the missing triadic interactions between (resolved) velocity and (filtered-out) scalar modes in the viscous-convective subrange do not affect *directly* the large scales. Second, the magnitude of the subgrid term is shown to be extremely small, which makes it particularly susceptible to numerical errors associated with the scalar transport scheme. *A posteriori* tests indicate that upwinded schemes, generally used for LES in complicated geometries, are sufficiently dissipative to overwhelm any contribution from the subgrid term. This renders the subgrid term superfluous, and as a result, VR-SF simulations run without subgrid scalar flux models are able to preserve large scale transport characteristics with remarkable accuracy. © *2013 AIP Publishing LLC*. [http://dx.doi.org/10.1063/1.4807061]

I. INTRODUCTION

The Schmidt number (Sc), defined as the ratio of the kinematic viscosity of a fluid (ν) to the molecular diffusivity of a scalar ($\mathcal{D}$), is the dimensionless quantity used to characterize scalar mixing in fluids. Batchelor, in his 1959 paper,[1] deduced that for low diffusivity passive scalars ($Sc \gg 1$), the smallest turbulent length scale of importance to the scalar field dynamics (the Batchelor scale: η_B) depends solely on the Kolmogorov length scale ($\eta = (\nu^3/\epsilon)^{1/4}$, where ϵ is the mean dissipation rate, and ν is the kinematic viscosity) and the Schmidt number:

$$\eta_B = \eta \cdot Sc^{-1/2}. \tag{1}$$

Batchelor further predicted that at extremely high Schmidt numbers, there must exist an intermediate range of wavenumbers (κ), now referred to as the "**viscous-convective subrange**." The fluid viscosity heavily influences scalar transport in this subrange, but the scalar diffusivity does not yet play an appreciable role. Batchelor went on to show that the scalar spectrum should exhibit a κ^{-1} scaling in this subrange. Several attempts have been made to verify this power law, but disagreement remains over its validity. Certain experiments and simulations support the scaling,[2–5] whereas others contradict it.[6–8] There even exist certain theoretical objections to the κ^{-1} scaling, based on the requirement of boundedness of the scalar variance.[9]

---

a)Electronic mail: sverma@caltech.edu
b)Electronic mail: g.blanquart@caltech.edu

    25, 055104-1

Simulations conducted to date with the goal of studying Batchelor's scaling law have been limited in scope by the availability of computational power. The few high Schmidt number datasets that are available are limited to either a very low Reynolds number, or to a relatively modest Schmidt number. For example, some of the best available combinations of Reynolds and Schmidt number simulations have been run at $Re_\lambda = 8$, $Sc = 1024$ by Yeung et al.,[3] and $Re_\lambda = 140$, $Sc = 64$ by Donzis et al.[5] The reason is the stringent requirement that the Batchelor scale imposes on grid resolution in numerical simulations, although recent developments based on compact finite-difference schemes[10] bring promise of some relief from a computational point of view. Commonly used guidelines[3] suggest that keeping $\kappa_{max}\eta_B \geq 1.5$, where κ_{max} is the largest available wavenumber determined by the grid resolution, ensures a fully resolved scalar field. Based on this criterion, a typical direct numerical simulation (DNS) of soot transport in air at a moderate $Re_\lambda = 100$ and $Sc = 1000$ would require on the order of $10\,000^3$ grid points for full resolution. The largest DNS that have been run to date on supercomputers[11] have not exceeded 4096^3 in grid resolution. The required resolution for soot transport thus represents almost two orders of magnitude increase in computational expense over the current state-of-the-art.

Both the Reynolds number and the Schmidt number can be increased by resorting to Large Eddy Simulation (LES), which alleviates the large cost of DNS to some extent. LES does not resolve the smallest physical scales, which results in a significantly relaxed grid resolution requirement. The drawback of using LES though is that the effect of the unresolved scales (called the "subgrid scales") on the resolved scale ("supergrid scale") dynamics must be modeled through an additional term in the Navier-Stokes equations. Construction of these LES models relies heavily on results from theoretical analysis, DNS, and experimental observation, all of which pose significant challenges at high Schmidt numbers. As a result, very limited amount of work relating to high Schmidt number scalar transport has been conducted to date using LES.[4,12–15]

The objective of the work presented in this paper is to explore options that may help close the gap that currently exists between experimental and numerical work. More precisely, our goal is to investigate the possibility to perform simulations that are less expensive than traditional DNS and yet do not possess the drawbacks of LES. Towards that goal, we take advantage of the large scale-separation between the Kolmogorov and Batchelor scales to perform *velocity-resolved, scalar-filtered (VR-SF) simulations*. We exploit the wide scale separation between η_B and η to our advantage by using an LES-type filter of width Δ such that $\eta_B \ll \Delta \ll \eta$ ($\eta_B \ll \Delta$ being a desirable rather than a necessary condition for minimizing simulation cost). One such filter placement, corresponding to the vertical line $\kappa_c\eta = 10$, is shown in Fig. 1. Here κ_c represents the cutoff wavenumber for the filter, and all information at higher wavenumbers, i.e., to the right of a $\kappa_c\eta$ line, is filtered out. The end
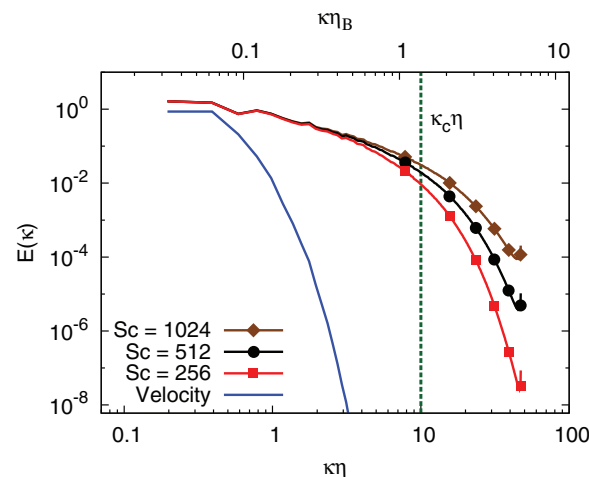

FIG. 1. 3D spectra for velocity and three different scalars. Data taken from DNS by Yeung et al.,[3] $\kappa\eta_B$ axis shown is for $Sc = 256$ ($\eta = 0.1958$).

result of this operation is a fully-resolved velocity field, but only a partially-resolved scalar field. This differs from standard LES since only the scalar field is filtered, whereas velocity fluctuations are completely resolved. In this paper, we will refer to such simulations as "velocity resolved, scalar filtered" simulations. A similar grid resolution criterion was used previously by Burton[4,15] for validating the performance of the "nonlinear LES" (n-LES) model in the viscous-convective subrange. We point out that the formulation of the n-LES model depends on *a priori* availability of the scalar spectrum at the subgrid scales (several model coefficients assume a κ^{-1} scalar spectrum). As will be shown later, the proposed VR-SF simulations are different in that no *a priori* behavior of the scalar spectrum is assumed. The only assumption is a scale separation between Kolmogorov and Batchelor scales, which is a direct outcome of the high Schmidt number of the scalar.

The consequence of filtering in the viscous-convective subrange and related discussion in terms of Batchelor's theory are presented first in Sec. II. The behavior of the subgrid terms computed using DNS data with respect to the filter width, the Reynolds number, and the Schmidt number is discussed in Sec. III. Furthermore, the subgrid terms have a limited range of influence on the supergrid scales, which can be attributed to the peculiar behavior of scalar spectral transfer in the viscous-convective subrange, as discussed in Sec. IV. Finally, Sec. V presents direct comparison of VR-SF runs to DNS data.

II. CONSEQUENCE OF FILTERING IN THE VISCOUS-CONVECTIVE SUBRANGE

A. Filtered transport equation

To observe the effect of filtering out the large wavenumbers, we start with the most general convection-diffusion equation, which is the conservation law governing the transport of a passive scalar. We use the symbol $\underset{\sim}{u}$ to represent the velocity vector, and z to represent any general passive scalar:

$$\frac{\partial z}{\partial t} + \nabla \cdot \left(\underset{\sim}{u} z \right) = \mathcal{D} \nabla^2 z. \tag{2}$$

This transport equation may be filtered using a homogeneous spatial filter of any general type. The most commonly used filtering kernels are the Sharp-Spectral filter, the Gaussian filter, and the Box filter. We use variables with an overtilde $\widetilde{(\cdot)}$ to represent filtered quantities:

$$\frac{\partial \tilde{z}}{\partial t} + \nabla \cdot \left(\widetilde{\underset{\sim}{u} z} \right) = \mathcal{D} \nabla^2 \tilde{z}. \tag{3}$$

The main drawback of the filtering operation is that Eq. (3) does not contain the flux term $\nabla \cdot \left(\underset{\sim}{\tilde{u}} \tilde{z} \right)$ that the filtered passive scalar transport equation actually solves for. This leaves a residual term in the filtered equation, which is referred to as the subgrid scalar flux (**SGF**) term:

$$\frac{\partial \tilde{z}}{\partial t} + \nabla \cdot \left(\underset{\sim}{\tilde{u}} \tilde{z} \right) = \mathcal{D} \nabla^2 \tilde{z} - \nabla \cdot \left(\widetilde{\underset{\sim}{u} z} - \underset{\sim}{\tilde{u}} \tilde{z} \right), \tag{4}$$

$$SGF = \widetilde{\underset{\sim}{u} z} - \underset{\sim}{\tilde{u}} \tilde{z}. \tag{5}$$

The SGF represents the effect of the smallest scales on the larger scales, which is not accounted for by the filtered equation. These effects arise from triadic interactions between scalar and velocity modes at large wavenumbers that then feed into the transport process at lower wavenumbers. These interactions are discussed in more detail in Sec. IV.

To assess the effect of filtering with a Sharp-Spectral filter, we write the velocity in terms of its Fourier modes:

$$\underset{\sim}{u}(\underset{\sim}{x}) = \sum_{|\underset{\sim}{\kappa}|=0}^{N/2} \widehat{\underset{\sim}{u}}(\underset{\sim}{\kappa}) e^{i \underset{\sim}{\kappa} \cdot \underset{\sim}{x}}. \tag{6}$$

Given that the cutoff wavenumber κ_c is set to a sufficiently large value ($\kappa_c \gg 1$), the subfilter velocity fluctuation amplitude (i.e., the subfilter velocity Fourier coefficients) can be approximated to be zero.

This is in accordance with the extremely low kinetic energy content at high wavenumbers. Thus, the filtered velocity resembles very closely the unfiltered velocity ($\widetilde{\underline{u}} \approx \underline{u} : \forall \kappa_c \eta \gg 1$), and can be expressed as follows in terms of the Fourier modes:

$$\underline{u}(\underline{x}) \approx \sum_{|\underline{\kappa}| \leq \kappa_c} \widehat{\underline{u}}(\underline{\kappa}) e^{i\underline{\kappa}\cdot\underline{x}}. \tag{7}$$

We can further argue that since the majority of the kinetic energy is concentrated at the lower wavenumbers, it can be assumed that the velocity field is spatially uniform, *within the filter width*, for very high cutoff wavenumbers. The same argument does not apply to the scalar quantity z or to the flux uz, since the scalar spectrum may retain a considerable amount of energy at high wavenumbers (Fig. 1).

Using these assumptions, combined with the fact that we are using a homogeneous filter, the two terms in the SGF simplify to

$$\widetilde{\underline{u}z} \approx \underline{u}\widetilde{z} \quad \text{and} \quad \widetilde{\underline{u}}\widetilde{z} \approx \underline{u}\widetilde{z}, \tag{8}$$

which in turn leads to

$$SGF = \widetilde{\underline{u}z} - \widetilde{\underline{u}}\widetilde{z} \approx 0. \tag{9}$$

Equation (9) suggests that neglecting subgrid information would have limited adverse effect on supergrid scale dynamics, assuming that we place the filter cutoff κ_c at a sufficiently large wavenumber. Stated differently, a subgrid scale model may not be necessary if $\kappa_c \eta \gg 1$. The result in Eq. (9), although obtained independently, was pointed out earlier by Calmet and Magnaudet.[12] The idea of no SGF model appears similar in principal to Implicit-LES (ILES).[16] The similarities and differences between the two methods will be discussed later in the paper (Sec. V A).

B. Assumption of locally uniform velocity

The principal assumption made in Eq. (8) is that the velocity field can be treated to be uniform in space with respect to the filtering operation. We plot in Fig. 2 a single component of the velocity vector and the corresponding scalar flux from one of the DNS datasets used for the *a priori* analysis. The inset shows a magnified region of the plot along with the characteristic filter width ($\Delta = \pi/\kappa_c$) in physical space, corresponding to a filter cutoff wavenumber of $\kappa_c \eta = 10$. Within the confines of the filter width, the low wavenumber dominated velocity signal (u) appears to be virtually a flat line, whereas the flux signal (uz) retains considerable curvature. We can therefore justify treating the velocity signal to be locally uniform in space, over the width of the filtering kernel, on condition that the cutoff wavenumber is sufficiently large (i.e., $\kappa_c \eta \gg 1$).
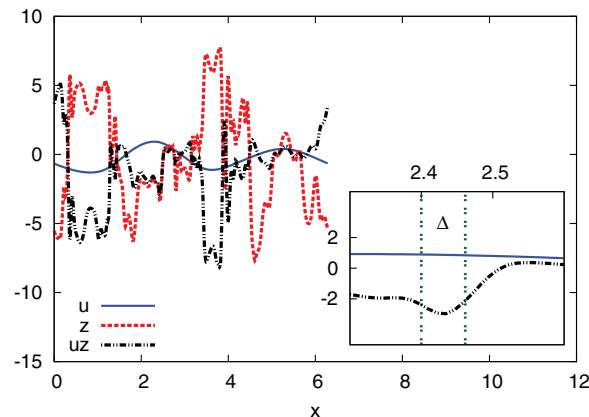

FIG. 2. Plot of the velocity, scalar, and the scalar flux along a line-cut across the DNS field for Case 5. Inset shows magnified view with effective filter width Δ corresponding to $\kappa_c \eta = 10$.

TABLE I. Baseline DNS datasets used for *a priori* analysis.

Case	N	Re_λ	Sc	ν	η	$\kappa_{max}\eta$
1[a]	192	8	64	0.1590	0.1285	12
2[a]	384	8	256	0.1590	0.1285	24
3[b]	512	8	256	0.1590	0.1958	48
4[b]	512	8	512	0.1590	0.1958	48
5[b]	512	8	1024	0.1590	0.1958	48
6[a]	512	30	64	0.0200	0.0460	12
7[c]	2048	140	64	0.0028	0.0114	11

[a]Present work with finite difference solver.[17]
[b]Data source: Yeung *et al.*[3]
[c]Data source: Donzis *et al.*[5]

This view of locality is certainly not robust, since the Gaussian and Sharp-Spectral filtering kernels are non-local in physical space. However, the rapid attenuation of the filtering kernels in physical space, away from the filtering location, makes this a reasonable assumption. The approximation used in Eq. (8) becomes more accurate at higher κ_c owing to a decrease in the filter width Δ and the corresponding faster attenuation of the filtering kernels.

We would like to point out that this approximation does not conflict with the assumptions made by Batchelor in the derivation of the κ^{-1} scaling.[1] Batchelor assumed that at sufficiently small scales, material "blobs" of the scalar are acted upon by essentially constant strain rates ($\gamma \sim (\epsilon/\nu)^{1/2}$) that are inversely proportional to the Kolmogorov time scale ($\tau_\eta = (\nu/\epsilon)^{1/2}$). This suggests that the majority of the deformation of scalar blobs (which may be much smaller in size than the Kolmogorov length scale) is caused by Kolmogorov sized eddies. With a filter width located in the viscous-convective subrange ($\kappa_c\eta \gg 1$), these Kolmogorov sized eddies, along with the accompanying constant straining motion, are fully resolved in the proposed VR-SF simulations.

III. *A PRIORI* TESTING

The behavior of the SGF magnitude, in particular its dependence on the Reynolds and the Schmidt numbers, is analyzed by filtering DNS data obtained from homogeneous isotropic turbulent simulations ("baseline data"). The simulation parameters along with the source of the data are listed in Table I. The results of the analysis were found to be independent of the numerical solver used to perform the simulation. The baseline datasets are filtered using the Sharp-Spectral filter, and the consequences of using other filtering kernels are discussed in Appendix A.

A. Filtering methodology

Since the SGF requires us to take the product of two terms, it is necessary to take additional precaution to ensure that aliasing from wavenumbers greater than κ_{max} does not impact the calculations. The SGF terms are dealiased in accordance with Orszag's "two-thirds truncation rule."[18] More specifically, the Fourier components corresponding to the upper third of the wavenumbers are discarded prior to performing any calculations. This operation is equivalent to filtering with the Sharp-Spectral filter at a low-pass cutoff wavenumber of $\frac{2}{3}\kappa_{max}$. We shall refer to the resulting output as "truncated data." We clarify here that the aliasing error in question arises during the postprocessing of the data, and is not associated with the DNS dataset itself. Equation (10) presents a schematic view of the steps followed, with "FFT" denoting the Fast Fourier Transform, and "IFFT" denoting the Inverse Fast Fourier Transform. The terms with the overhat $\widehat{(\cdot)}$ represent Fourier coefficients, and the subscript "d" indicates truncated data:

$$\underset{\sim}{u} \xrightarrow{FFT} \widehat{\underset{\sim}{u}} \xrightarrow{Truncation} \widehat{\underset{\sim}{u}}_d \xrightarrow{IFFT} \underset{\sim}{u}_d$$

$$z \xrightarrow{FFT} \widehat{z} \xrightarrow{Truncation} \widehat{z}_d \xrightarrow{IFFT} z_d. \qquad (10)$$

To obtain the first term in the SGF ($\widetilde{\underset{\sim}{u}z}$), the two truncated quantities are multiplied, followed by the operations shown below:

$$\underset{\sim}{u}_d z_d \xrightarrow{FFT} \widehat{\underset{\sim}{u}_d z_d} \xrightarrow{Filter} \widehat{\widetilde{\underset{\sim}{u}_d z_d}} \xrightarrow{IFFT} \widetilde{\underset{\sim}{u}_d z_d}. \tag{11}$$

To obtain the second term in the SGF ($\tilde{u}\tilde{z}$), the following operations are first performed on the truncated data,

$$\underset{\sim}{u}_d \xrightarrow{FFT} \widehat{\underset{\sim}{u}}_d \xrightarrow{Filter} \widehat{\widetilde{\underset{\sim}{u}}}_d \xrightarrow{IFFT} \tilde{u}_d$$

$$z_d \xrightarrow{FFT} \widehat{z}_d \xrightarrow{Filter} \widehat{\widetilde{z}}_d \xrightarrow{IFFT} \tilde{z}_d, \tag{12}$$

and then the filtered quantities are multiplied to get $\tilde{u}_d \tilde{z}_d$. From this point forward, we shall drop the subscript "d" for convenience, and assume that truncated and dealiased data are used, unless otherwise stated.

B. Qualitative analysis

To observe the degree of correlation between $\widetilde{\underset{\sim}{u}z}$ and $\tilde{u}\tilde{z}$, Fig. 3 shows contours of the Joint Probability Density Function (JPDF) at various filter cutoffs, with the color map shown on the right
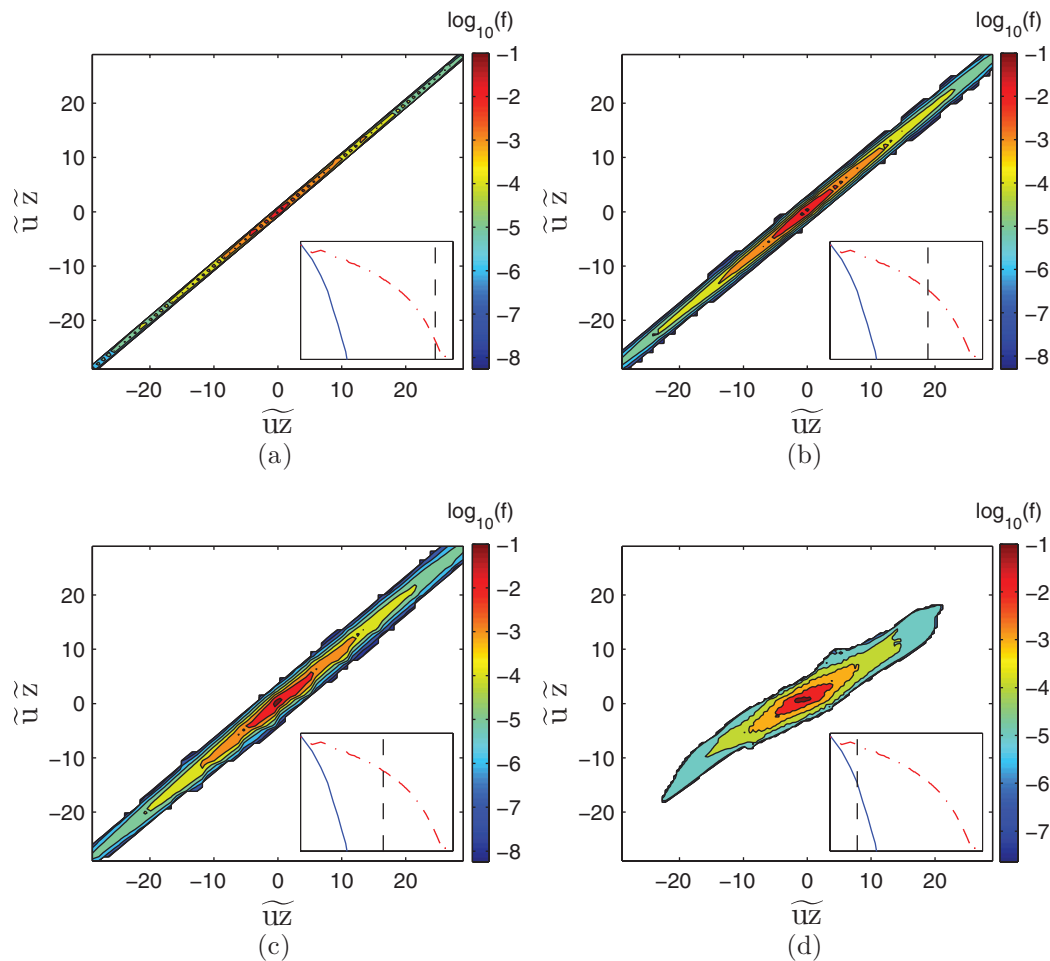

FIG. 3. Joint probability density function for the two terms in the SGF at various sharp filter cutoff wavenumbers. Whitespace indicates absence of data points. The inset figures show the corresponding location of the cutoff with respect to the velocity and scalar spectra. Data taken from baseline Case 5 (Table I). Only the y and z components of the scalar flux have been used (Appendix B). (a) $\kappa_c \eta = 33$. (b) $\kappa_c \eta = 10$. (c) $\kappa_c \eta = 6$. (d) $\kappa_c \eta = 1$.

of each frame. Any scatter in the direction perpendicular to the 45°diagonal represents the error introduced by filtering, which should be accounted for by the SGF term.

Figure 3(a) with $\kappa_c \eta = 33 = \frac{2}{3}\kappa_{max}\eta$ serves as the baseline case, since dealiasing reduces the largest wavenumber available in the data. We can clearly identify that this case has no error, based on the perfect correlation between the two quantities. Figure 3 suggests that the relative differences between $\widetilde{\underset{\sim}{u}z}$ and $\tilde{\underset{\sim}{u}}\tilde{z}$ increase as $\kappa_c\eta$ is moved to lower values, since a wider JPDF is indicative of increasing disparity between the two terms in the SGF. This is expected since a lower $\kappa_c\eta$ corresponds to neglecting a greater proportion of the information available at higher wavenumbers. Nevertheless, the shape of the JPDF remains fundamentally the same throughout the viscous-convective subrange (Figs. 3(b) and 3(c)) and the increase in the error in assuming SGF = 0 is relatively modest compared to the large savings in computational cost that can be realized by using VR-SF. In the limit when $\kappa_c\eta = 1$, the JPDF no longer adheres to the 45°diagonal, which suggests that the magnitude of the subgrid term is substantial.

C. Magnitude of the SGF term

Following the qualitative analysis in Subsection III B, we now analyze quantitatively the effects of filter width, Reynolds number, and Schmidt number on the magnitude of the SGF term.

1. Definitions

Using Eq. (5) in conjunction with the symbol $\boldsymbol{SGF}_{i,j,k}$ to represent the calculated value of the SGF at grid location $(i, j, k) \in [1, N]^3$ (where N is the number of grid points in each direction), we get

$$SGF_{i,j,k} = \widetilde{\underset{\sim}{u}z}_{i,j,k} - \tilde{\underset{\sim}{u}}_{i,j,k}\tilde{z}_{i,j,k}.\tag{13}$$

Then, the L_2 norm ($|\boldsymbol{SGF}|$) can be written as

$$|SGF| = \left(\frac{1}{N^3}\sum_{i,j,k=1}^{N}(SGF_{i,j,k})^2\right)^{\frac{1}{2}}.\tag{14}$$

Normalizing this L_2 norm using the standard deviations for the truncated velocity ($\sigma_{\underset{\sim}{u}}$) and scalar ($\sigma_z$) fields, we arrive at a suitable definition for the non-dimensional relative magnitude $\boldsymbol{m}$:

$$m = \frac{|SGF|}{\sigma_{\underset{\sim}{u}}\cdot\sigma_z}.\tag{15}$$

Since the SGF as defined in Eq. (13) is a vector quantity, we can calculate m component-wise as follows:

$$m = \frac{1}{\sigma_z\sqrt{2}}\cdot\sqrt{\left(\frac{|SGF|_v}{\sigma_v}\right)^2 + \left(\frac{|SGF|_w}{\sigma_w}\right)^2}.\tag{16}$$

The u component of the SGF has been excluded in this definition, since the flux component in the direction of the imposed mean scalar gradient differs systematically from the other two components (Appendix B).

2. Dependence on $\kappa_c\eta$ and Sc

Figure 4 shows the variation of m with $\kappa_c\eta$ when a Sharp-Spectral filter was used for filtering the baseline datasets. We can identify two regions of distinct behavior with respect to $\kappa_c\eta$. For $\kappa_c\eta < 3$, the magnitude grows very rapidly with decreasing κ_c, and is independent of the Schmidt number. This distinctive change in SGF behavior happens since we are neglecting useful velocity information close to the Kolmogorov length scale. As was discussed in Sec. II B, these velocity modes play a crucial role during scalar transport even in the viscous-convective subrange. The non-ideal shape of
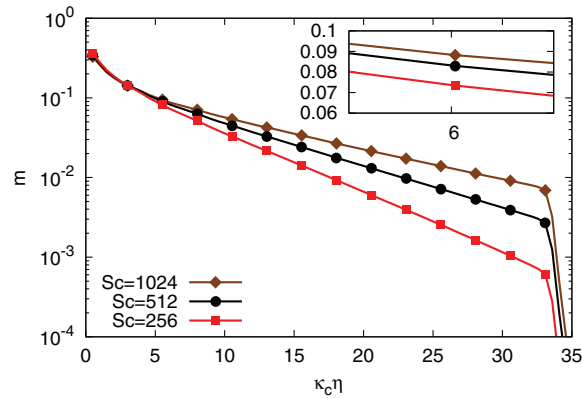
FIG. 4. Relative magnitude vs. sharp filter cutoff wavenumber. Data taken from baseline Cases 3, 4, and 5, averaged over 4 stationary snapshots ($t/\tau_{eddy} = 5.7$, 10, 11.6, and 13.8).

the JPDF shown in Fig. 3(d) is consistent with these results, however, we must be mindful of the fact that few Fourier modes remain for the case shown at $\kappa_c \eta = 1$.

For $\kappa_c \eta > 5$, we observe a slower, exponential drop in relative magnitude of the SGF term with the selected cutoff wavenumber. The decay rate in this region is dependent on the Schmidt number; higher Schmidt numbers result in a smaller slope. This behavior is expected since, for the same selected $\kappa_c \eta$, we ignore a larger proportion of the useful information available at higher Schmidt numbers. We can infer this from Fig. 1, where the spectrum for a smaller Schmidt number scalar decays faster than that for a larger Schmidt number scalar.

An important trend to note from Fig. 4 is that the magnitude increase, quantifiable by the vertical shift of the SGF magnitude curve, slows down with increasing Schmidt number. For instance, at approximately $\kappa_c \eta = 6$, the relative magnitude increases by 1% going from $Sc = 256$ to $Sc = 512$, but only by another 0.5% when going from $Sc = 512$ to $Sc = 1024$. One would thus hope that the SGF magnitude curve tends towards an asymptotic shape at very high Schmidt numbers, thereby making the computed magnitude of the SGF term independent of the Schmidt number.

Finally, the rapid decrease in the SGF magnitude for filtering beyond $\kappa_c \eta = 33$, which is the value for $\kappa_{max}\eta$ after dealiasing for the case shown, serves as a check for the *a priori* analysis. Filtering beyond the dealiasing limit merely removes noise from the data and the two terms that constitute the SGF are now exactly equal.

3. Dependence on Re$_\lambda$

To determine the effect of changing the Reynolds number, we compare the normalized magnitude of the SGF term in Fig. 5 at a fixed Schmidt number ($Sc = 64$) and at three different Reynolds numbers. With the current normalization of the magnitude of the SGF term introduced in Eq. (16), the results are dependent on the Reynolds number; a higher Reynolds number results in lower magnitude. However, when the definition of m is altered to rescale with the Kolmogorov velocity scale ($u_\eta \sim (\epsilon\eta)^{(1/3)}$) instead of σ_u, the curves collapse almost perfectly (Fig. 5(b)),

$$m = \frac{1}{u_\eta \sigma_z \sqrt{2}} \cdot \sqrt{|SGF|_v^2 + |SGF|_w^2}. \tag{17}$$

This collapse is not unexpected and confirms that it is indeed the small velocity scales that are important for determining m. Furthermore, we can conclude from the collapse that the magnitude of the SGF, when appropriately normalized, behaves independently of the Reynolds number for high Schmidt number mixing.
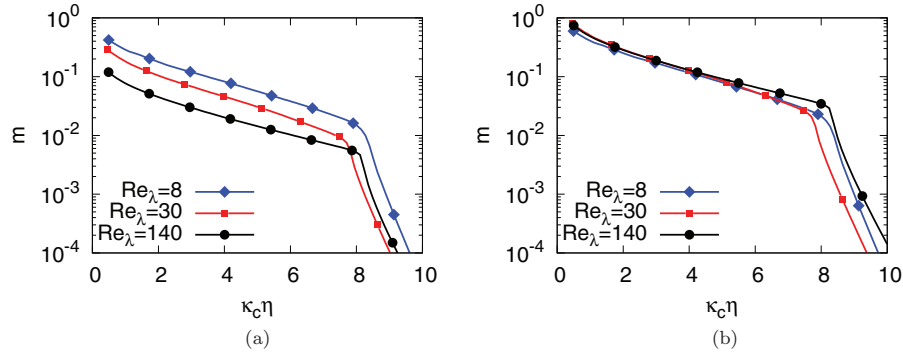
FIG. 5. Comparison of m vs. $\kappa_c \eta$ plots for Sc = 64 and three different Reynolds numbers. Baseline Cases 1, 6, and 7. (a) m as defined in Eq. (16). (b) Rescaled m as defined in Eq. (17).

IV. SCALAR ENERGY TRANSFER

Filtering the scalar transport equation alters the transfer of scalar energy from the large scales to the small scales. As suggested in Secs. II and III, this transfer is fundamentally different in the viscous-convective subrange when compared to the inertial subrange. Inspecting the transfer spectrum can provide insight into how triadic interactions among velocity and scalar modes in certain wavenumber ranges influence transport at all other wavenumbers. This is central in understanding the role of the SGF term in the viscous-convective subrange.

A. The scalar transfer spectrum

The relevant term corresponding to spectral transfer in the scalar energy equation is obtained by first taking the Fourier transform of the transport equation. This is followed by multiplication with the conjugate of the scalar Fourier coefficient ($\widehat{z}^*(\underset{\sim}{\kappa})$). Finally, the scalar transfer spectrum $T(k)$ is computed by averaging the convective term over spherical wave-shells. This averaging operation is denoted by angled brackets. All products involved are dealiased as discussed in Sec. III A:

$$T(\kappa) = \left\langle -2Re\left(\widehat{z}^*(\underset{\sim}{\kappa})\ \widehat{\underset{\sim}{u}\cdot\nabla z}(\underset{\sim}{\kappa})\right)\right\rangle \tag{18}$$

$$= \left\langle 2\underset{\sim}{\kappa}\cdot Im\left(\widehat{z}^*(\underset{\sim}{\kappa})\int_{\underset{\sim}{\kappa}=\underset{\sim}{p}+\underset{\sim}{q}}\widehat{\underset{\sim}{u}}(\underset{\sim}{p})\widehat{z}(\underset{\sim}{q})d\underset{\sim}{p}\right)\right\rangle.$$

The expression obtained involves triadic interactions between scalar and velocity modes, which contribute to the scalar flux mode associated with wavenumber vector $\underset{\sim}{\kappa}$. We would like to point out that during scalar transport, each velocity mode (wavenumber vector $\underset{\sim}{p}$) interacts with each scalar mode (wavenumber vector $\underset{\sim}{q}$), and the resultant corresponds to a new mode with wavenumber vector $\underset{\sim}{p}+\underset{\sim}{q}$.

It is instructive to decompose the transfer spectrum $T(\kappa)$ into contributions from various velocity ($V(\kappa|p)$) and scalar ($S(\kappa|q)$) modes[19] as follows:

$$V(\kappa|p_A) = \left\langle 2\underset{\sim}{\kappa}\cdot Im\left(\widehat{z}^*(\underset{\sim}{\kappa})\int_{|\underset{\sim}{p}|\epsilon A}\widehat{\underset{\sim}{u}}(\underset{\sim}{p})\widehat{z}(\underset{\sim}{\kappa}-\underset{\sim}{p})d\underset{\sim}{p}\right)\right\rangle, \tag{19}$$

$$S(\kappa|q_A) = \left\langle 2\underset{\sim}{\kappa}\cdot Im\left(\widehat{z}^*(\underset{\sim}{\kappa})\int_{|\underset{\sim}{q}|\epsilon A}\widehat{\underset{\sim}{u}}(\underset{\sim}{\kappa}-\underset{\sim}{q})\widehat{z}(\underset{\sim}{q})d\underset{\sim}{q}\right)\right\rangle. \tag{20}$$
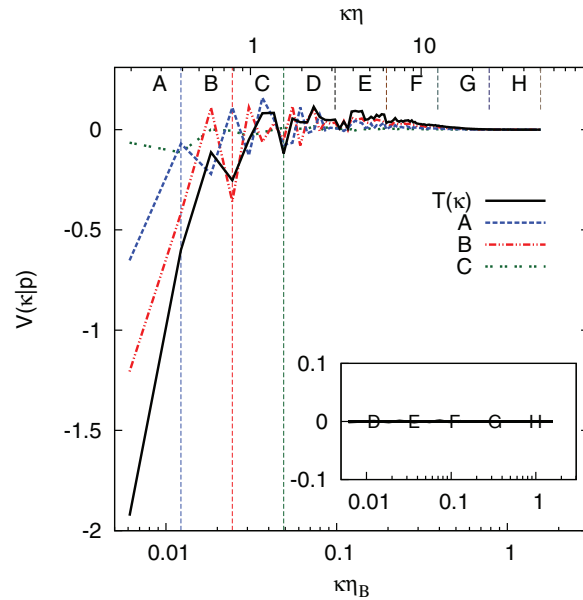
FIG. 6. Contribution of velocity modes $V(\kappa|p)$ (lines A through H) to the scalar transfer spectrum $T(\kappa)$ (Eq. (19)). Inset shows velocity modes for wavenumber ranges D and higher.

The combined contribution of these modes must add up to give back the transfer spectrum:

$$T(\kappa) = \sum_p V(\kappa|p) = \sum_q S(\kappa|q). \qquad (21)$$

$V(\kappa|p)$ and $S(\kappa|q)$ are plotted for baseline Case 5 in Figs. 6 and 7, respectively, using logarithmically spaced ranges for the contributing modes. The data shown were taken from baseline Case 5 (Table I), averaged over 4 stationary snapshots ($\tau_{eddy} = 5.7, 10, 11.6,$ and 13.8). Bandpass filtering of the pertinent variables was done using the Sharp-Spectral filter. Figure 6 indicates that velocity contributions from higher wavenumber ranges (regions D and above) are almost zero, and hence play virtually no part in the spectral transfer of scalar energy.
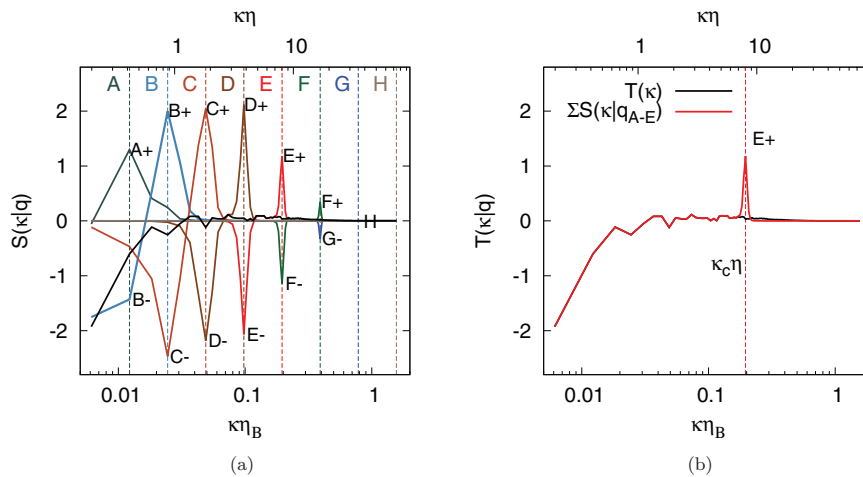
FIG. 7. Contribution of scalar modes $S(\kappa|q)$ to the scalar transfer spectrum $T(\kappa)$ (Eq. (20)). $S(\kappa|q)$ from wavenumber ranges A through E are summed up in (b) to emulate the effect of filtering with a Sharp-Spectral filter (at $\kappa_c \eta \approx 6$). (a) Decomposition of $T(\kappa)$ (solid black line) into $S(\kappa|q)$. (b) Comparison of full transfer spectrum $T(\kappa)$, and that obtained after filtering scalar modes beyond $\kappa_c \eta \approx 6$.
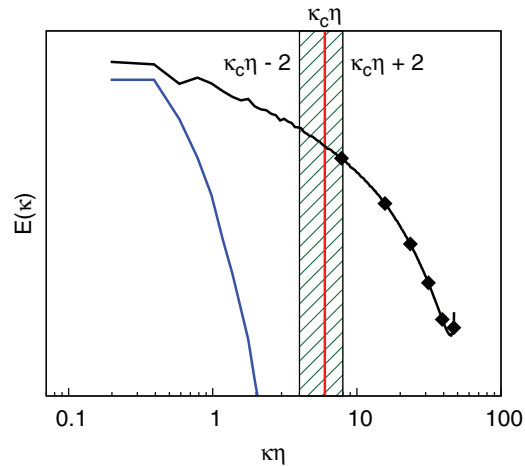
FIG. 8. Locality of triadic interactions for high Schmidt number cases (as discussed in Eq. (22)). The hatched region corresponds to all non-zero contributions from scalar-velocity triadic interactions to the transfer term at wavenumber κ_c.

We now take a closer look at the scalar mode contributions in Fig. 7(a). We note that for scalar modes belonging to higher wavenumber ranges (e.g., regions D and above), the effective triadic interactions become extremely local, having a noticeable effect only on the immediately neighboring ranges. To be more specific, scalar modes belonging to lower wavenumber ranges contribute to transfer in non-neighboring ranges (for instance, scalar modes in range C affect transfer in ranges A, B, C, and D). However, scalar modes in range E affect transfer only in the immediately neighboring ranges (D, E, and F).

This locality of triadic interactions is not surprising, and is solely related to the faster decay of the velocity spectrum compared to the scalar spectrum (Fig. 1) (it is not a consequence of bandpass filtering). For the sake of simplicity, let us assume that the velocity Fourier coefficients beyond $\kappa\eta = 2$ are exactly zero. Assuming $\widehat{\underset{\sim}{u}}(\underset{\sim}{\kappa}) = 0$ for $|\underset{\sim}{\kappa}\eta| > 2$ helps us simplify the convolution integral in Eq. (18), which now reads

$$T(\kappa) = \left\langle 2\underset{\sim}{\kappa} \cdot Im \left(\widehat{z}^*(\underset{\sim}{\kappa}) \int_{|\underset{\sim}{p}| < \frac{2}{\eta}} \widehat{\underset{\sim}{u}}(\underset{\sim}{p}) \widehat{z}(\underset{\sim}{\kappa} - \underset{\sim}{p}) d\underset{\sim}{p} \right) \right\rangle. \tag{22}$$

The only difference between Eqs. (18) and (22) is that the velocity modes are now restricted to those with non-zero amplitudes. Equation (22) communicates that among all mathematically-possible triadic interactions between velocity and scalar modes, it is only the interactions within a relatively narrow band around $|\underset{\sim}{\kappa}|$ (in this case, $\kappa \pm 2/\eta$) that result in a non-zero contribution to the transfer term at this wavenumber. This is depicted schematically in Fig. 8, and is a direct result of the large scale separation between η and η_B. The locality of the triadic interactions is indeed valid only at high Schmidt numbers and in the viscous-convective subrange, as may be confirmed by the non-local behavior of decomposed transfer spectra ($S(\kappa|q)$) for low Schmidt number scalars.[19]

B. Implications for VR-SF simulations

We now utilize the local nature of triadic interactions to analyze the cascade of scalar energy down to successively higher wavenumbers, and how it relates to filtering in the viscous-convective subrange. Scalar modes belonging to a particular wavenumber range, for instance E (Fig. 7(a)), extract energy from the range to the immediate left (spike E−), and deposit energy at the end of the range in question (spike E+). At high wavenumbers, this deposition is balanced almost exactly by the extraction of energy by scalar modes belonging to the wavenumber range on the immediate right (spike F−). The near-perfect balance of energy transfer among neighboring wavenumber ranges

TABLE II. VR-SF simulation parameters.

Case	N	Re_λ	Sc	ν	η	$\kappa_c \eta$	$\kappa_c \eta_B$
A	128	8	1024	0.159	0.1290	8	0.250
B	256	8	1024	0.159	0.1283	16	0.500
C	512	48	1024	0.010	0.0272	7	0.218

indicates that triadic interactions originating from these high wavenumber scalar modes cannot impact *directly* the transfer at intermediate (i.e., non-neighboring) wavenumbers.

Filtering the data (as done in VR-SF with a low pass filter) may still have an *indirect* effect on the scalar transfer spectrum. For demonstration purposes, we suppose that the low-pass filter cutoff is placed at the boundary of regions E and F. The resulting transfer spectrum after filtering, shown in Fig. 7(b), is obtained by summing the scalar mode contributions from wavenumber ranges A through E. The excellent agreement between the full and filtered spectra at low and intermediate wavenumbers yet again emphasizes the minimal influence of high wavenumber modes. However, we note that there is no longer a cancellation of the E+ spike from an F− spike since the F modes have been filtered out. The E+ spike, if left unchecked, can lead to a pile-up of scalar energy at the large wavenumbers. This could have an indirect effect on the scalar transfer, especially for spectral and scalar energy conserving transport schemes. The analysis of the impact of possible discretization errors on scalar mixing and the energy spectrum is the subject of Sec. V.

As a side note, we mention that the pile-up of energy discussed in this section is often observed in scalar spectra obtained using spectral transport schemes. The pile-up manifests as an upturned peak at the end of the spectrum (e.g., Fig. 1), since any spatial discretization removes higher wavenumber modes, which would otherwise have led to energy cascading down to even smaller scales.

V. VR-SF SIMULATIONS

The essence of the VR-SF technique lies in the assumption that running simulations on a semi-resolved grid is equivalent to filtering with a Sharp-Spectral filter. We now present results from VR-SF runs of homogeneous isotropic turbulence. The simulation parameters used for these VR-SF runs (Table II) resemble closely to those used in generating the baseline DNS data (Table I). This was necessary to allow direct comparisons with data from the baseline cases.

The velocity field for the VR-SF runs, as well as for baseline Cases 1, 2, and 6, was forced spectrally by injecting energy in a low wavenumber shell.[20] The scalar was maintained statistically stationary using an imposed uniform mean scalar gradient (Eq. (B2) with $G = 1$).

A. Impact of numerical discretization errors

In Secs. II–IV, we have found that the behavior of the SGF term in the viscous-convective subrange is very different from that in the inertial subrange (Sec. III C 2). We have also shown that the relative magnitude of the SGF term is very small for $\kappa_c \eta > 5$ (Fig. 4). Finally, in Sec. IV, we observed that the SGF does not have a direct impact on an overwhelming majority of the resolved scales. Based on these observations, one might wonder if the SGF term could be neglected altogether. Towards that goal, and in order to test for the impact of numerical discretization errors, we perform VR-SF simulations without an SGF (i.e., by setting SGF = 0), using high order upwinded convective (HOUC) schemes .[17,21]

Figure 9 shows results from simulation runs with increasing order of accuracy, namely, HOUC 3, 5, and 7. These results indicate that the scalar energy spectrum in the viscous-convective subrange is unaffected by the scheme used: the expected κ^{-1} slope is unchanged. Using higher order schemes results in merely a larger extent of the constant slope. This is expected since a higher order scheme is characterized by lower artificial numerical diffusivity and leads to smaller errors at the large wavenumbers. Nevertheless, it is important to note that the low numerical diffusion associated with
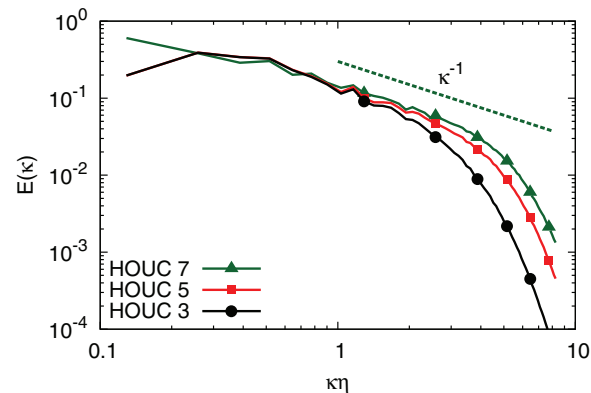
FIG. 9. Scalar spectra comparison for Case A (VR-SF: Table II) run with 3 different upwind convective schemes.

even high order upwinded schemes (5th and 7th order, as used in our VR-SF simulations) is sufficient to damp out the positive spike in the filtered transfer spectrum (akin to the E+ spike shown in Fig. 7(b)), thereby keeping the simulations stable. This suggests that no SGF terms are necessary when using non energy-conserving scalar schemes, as the numerical errors introduced by these schemes (albeit already small) remain larger than the magnitude of the SGF term.

Using the discrete derivative operator associated with upwind transport schemes as an energy sink may be considered to be a variant of the ILES approach.[16] Nevertheless, there are subtle differences in the working assumptions of the two methods. ILES often employs second order schemes with some form of flux-limiting, and the resulting leading-order truncation error terms are used as replacement for explicit subgrid models. On the contrary, VR-SF relies on physical arguments which indicate that the subgrid terms in high Schmidt number cases are very nearly zero for $\kappa_c\eta \gg 1$ (Sec. II A). The only task that remains in VR-SF is the damping of any possible energy pile-up as discussed in Sec. IV B. This damping may be carried out using *any* high order scheme that entails sufficient, but minimal numerical diffusion (so as to avoid disrupting spectral transfer at the intermediate scales), as opposed to being limited to the second order discrete operators specially tailored for use in ILES. Unlike ILES, VR-SF simulations may be performed with an energy-conserving scheme (such as a spectral scheme). In such a case, a model for the SGF term would be necessary to damp the energy pile-up close to the filter cutoff.

B. Comparison to DNS

Following the results in Subsection V A, all further VR-SF simulations are performed without a SGF term, and using the fifth order HOUC scheme. The results from the VR-SFs are compared to those from the corresponding baseline DNS dataset. The focus is on assessing the effectiveness of the technique in retaining expected physical behavior at the large scales, despite the fact that a majority of the relevant information at the higher wavenumbers has been neglected entirely.

Figures 10(a) and 10(b) show the energy spectra and energy dissipation spectra ($D(\kappa) = \mathcal{D}\kappa^2 E(\kappa)$) of the filtered scalar fields for different filter cutoffs. We observe that even the coarsest grid simulation ($\kappa_c\eta = 8$, $N = 128$) is in excellent agreement with the baseline data at the small wavenumbers (i.e., the large physical scales), and exactly matches the DNS scalar energy and dissipation spectra all the way up to $\kappa\eta = 3$. Nevertheless, there are some differences at higher wavenumbers, as is clearly evident from the dissipation spectra. This can be attributed to two elements. First, performing a simulation on a coarser mesh is not strictly equivalent to filtering the data with a Sharp-Spectral filter. The "underlying/effective" filter is most likely a combination of Spectral and Gaussian filters. Second, the effect of numerical diffusion is strongest at the smaller scales owing to large values of the scalar gradient. A non-diffusive scalar transport scheme would
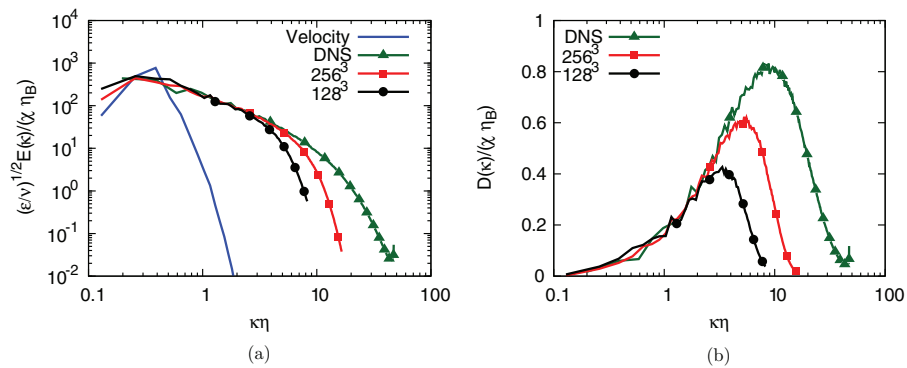
FIG. 10. Scalar spectra comparison for Cases A, B (VR-SF: Table II), and baseline Case 5 (DNS: Table I). The mean scalar dissipation rate (χ) used for the filtered runs was estimated from an unfiltered run using the finite difference solver. (a) Normalized scalar energy spectra. (b) Normalized scalar dissipation spectra.

show better agreement with the DNS result, but would still require energy damping at the highest wavenumbers as noted in Subsection V A.

C. Increasing the Re_λ

In order to obtain results comparable to experiments, simulations need to achieve a minimum of $Re_\lambda \approx 100$. Figure 11 shows scalar and velocity spectra from a VR-SF run at $Re_\lambda = 48$, Sc = 1024, and $\kappa_c \eta = 7$ (Case C). The scalar spectrum exhibits the expected κ^{-1} scaling in the viscous-convective subrange, all the way up to $\kappa \eta = 2$, beyond which the effects of numerical diffusion dominate. This result, along with those presented in Subsections V A and V B, reinforces the idea that the SGF terms can be safely modeled to be zero, without disrupting the turbulent transport process at the large scales. To capture correctly the behavior in the viscous-convective subrange, we simply need to ensure that $\kappa_c \eta \gg 1$, and that some form of mechanism exists for damping out energy pile-up close to the filter cutoff.

VI. SUMMARY AND CONCLUSION

In this paper, we have investigated the validity of performing velocity-resolved, scalar-filtered numerical simulations of high Schmidt number scalar turbulent transport. The conceptual basis of the technique relies on the observation that the velocity energy spectrum decays much more rapidly than the energy spectrum of a high Schmidt number scalar. Based on this observation, the contribution of
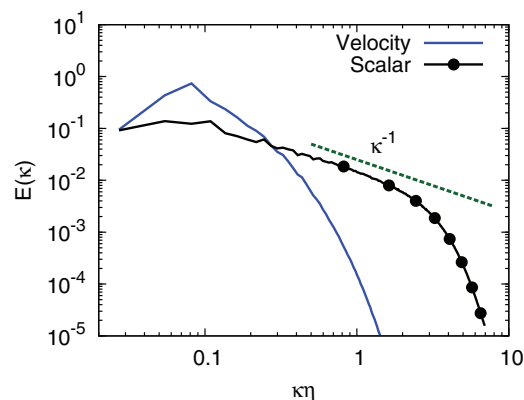

FIG. 11.   VR-SF run at $Re_\lambda = 48$, Sc = 1024, and $\kappa_c \eta = 7$ (Case C).

the subgrid scalar flux to the supergrid scalar dynamics has been shown (*a priori* and *a posteriori*) to be negligible at very large wavenumbers ($\kappa_c \eta \gg 1$). Thus, simulations that resolve sufficiently far into the viscous-convective subrange account for the majority of the effective scalar-velocity triadic interactions, thereby eliminating the need of a subgrid scale model for this purpose. Some form of energy damping is still required to prevent the build up of unphysical energy, and may be achieved through the use of discrete derivative operators that contain sufficient upwinding. In fact, the present results indicate that implementing a SGF model is not justified unless the numerical errors are shown explicitly to be smaller than the SGF term.

Simulations run using the technique outlined are shown to capture accurately the expected physical behavior at large scales, even in the absence of a subgrid model, so long as the filter cutoff is placed in the viscous-convective subrange. The substantial reduction in computational cost, coupled with the high fidelity of the technique makes VR-SF an ideal candidate for studying the transport and mixing of high Schmidt number scalars.

APPENDIX A: EFFECT OF USING VARIOUS FILTERING KERNELS

The *a priori* tests discussed in Secs. III B and III C were repeated using the Gaussian and Box filtering kernels. The resulting m vs. $\kappa_c \eta$ curves are compared (Fig. 12) with the appropriate SGF magnitude curve from Sec. III C, which was obtained using a Sharp-Spectral filter. The Gaussian and Box filters result in approximately an order of magnitude drop in the value of m. However, closer inspection reveals that the calculated subgrid term magnitude seems to be much too small, particularly at very low $\kappa_c \eta$ when the majority of the available information has been neglected. Another notable inconsistency is that the Gaussian and Box filters do not exhibit the expected rapid decrease in error beyond the dealiasing limit $\kappa_c \eta = 33$, at which point the SGF should theoretically become zero.

In order to investigate the cause of these anomalies, we make use of the filtered 1D flux energy spectra shown in Fig. 13. We can clearly see that for a moderate cutoff wavenumber ($\kappa_c \eta = 6$),
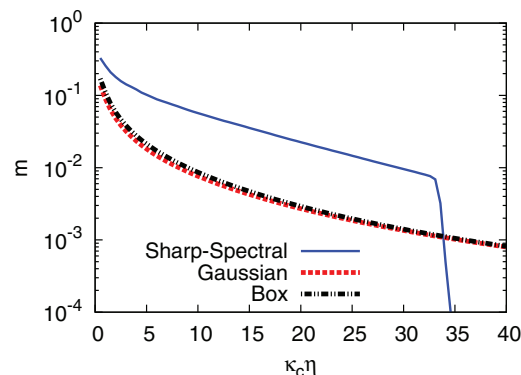

FIG. 12. m vs. $\kappa_c \eta$ plot with 3 different filtering kernels. Baseline Case 5 averaged over 4 stationary snapshots.
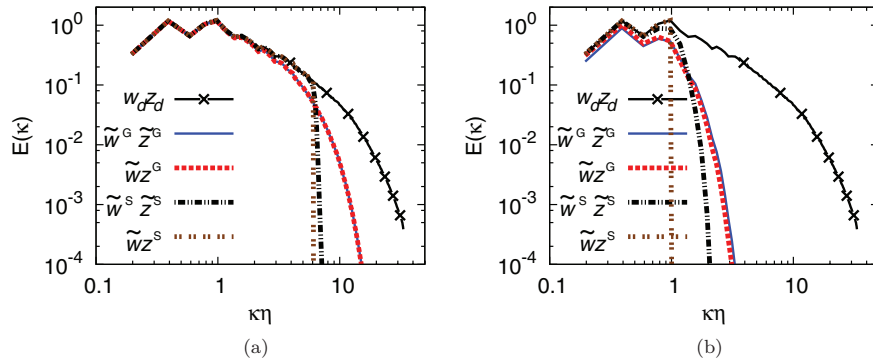
FIG. 13. Spectra comparison of $\widetilde{w}\tilde{z}$ and $\widetilde{wz}$ (z component only) using the Gaussian and Sharp-Spectral filtering kernels (baseline Case 5). Superscript "G" corresponds to filtering with the Gaussian filter, and superscript "S" corresponds to the Sharp-Spectral filter. (a) Filter cutoff at $\kappa_c\eta = 6$. (b) Filter cutoff at $\kappa_c\eta = 1$.

the Gaussian filtered spectra for the two SGF terms are virtually identical, but not so for the sharp filtered spectra. At very low cutoff ($\kappa_c\eta = 1$), the two Gaussian filtered spectra are still in very good agreement, whereas the Sharp-Spectral spectra are considerably dissimilar. The difference between $\widetilde{w}\tilde{z}$ and $\widetilde{wz}$ in physical space will, hence, be much smaller when using a Gaussian filter, resulting in an appreciably smaller value of m.

This "agreeable" behavior can be attributed to the gradual rolloff in the attenuation factor for the Gaussian filtering kernel, which results in extraneous contribution from wavenumbers beyond the specified cutoff. The continuous attenuation of the Gaussian and Box filters introduces a "smearing out" effect, which reduces the sharp differences that should theoretically exist between the two SGF terms. Due to this occurrence of "one error cancelling out another," the Gaussian and Box filters have been excluded from use in the *a priori* analysis.

APPENDIX B: ANISOTROPY DUE TO THE IMPOSED MEAN SCALAR GRADIENT

In order to mimic the mixing of scalars in experimental setups, the baseline datasets use an imposed mean scalar gradient in the transport equation. This maintains statistical stationarity and stops the spectrum from decaying. The modified transport equation is shown in Eq. (B2), and is obtained by decomposing the scalar into its mean and spatially fluctuating parts as follows:

$$Z = z + G \cdot x, \tag{B1}$$

where G represents the imposed mean scalar gradient in the x-direction, and scalar fluctuation is given by z. The transport equation shown in Eq. (2), under the assumption of incompressibility ($\nabla \cdot \underset{\sim}{u} = 0$), now becomes

$$\frac{\partial z}{\partial t} + \underset{\sim}{u} \cdot \nabla z = \mathcal{D}\nabla^2 z - uG. \tag{B2}$$

The additional source term (uG) is responsible for maintaining the variance at a constant level, but introduces anisotropy in the scalar field in the x-direction.[22,23] Upon inspection of the scalar fluxes (Figs. 14(a) and 14(b)) in the baseline data, it was found that the x-component (uz) has a non-negligible negative mean value and its probability density function (PDF) is skewed. In order to avoid unforseen complications that this large anisotropy in the baseline dataset might give rise to in the *a priori* analysis, we chose to use a combination of only the y and z components of the scalar flux. Figure 14(b) confirms that the combined PDF for the y and z fluxes (vz and wz) is indeed centered at zero.
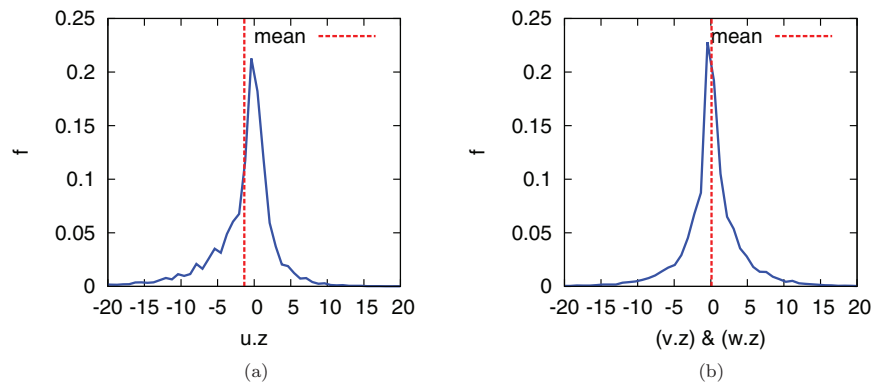
FIG. 14. Probability Density Function (PDF) of scalar flux components. Baseline Case 5 averaged over 4 stationary snapshots. (a) PDF of scalar flux in the *x*-direction. Mean value $= -1.34$. (b) Combined PDF of scalar flux in the *y* and *z* directions. Mean value $= 0.11$.

[1] G. K. Batchelor, "Small-scale variation of convected quantities like temperature in turbulent fluid. Part 1. General discussion and the case of small conductivity," J. Fluid Mech. **5**, 113 (1959).

[2] M. C. Jullien, P. Castiglione, and P. Tabeling, "Experimental observation of Batchelor dispersion of passive tracers," Phys. Rev. Lett. **85**, 3636 (2000).

[3] P. K. Yeung, S. Xu, D. A. Donzis, and K. R. Sreenivasan, "Simulations of three-dimensional turbulent mixing for Schmidt numbers of the order 1000," Flow, Turbul. Combust. **72**, 333 (2004).

[4] G. C. Burton, "The nonlinear large-eddy simulation method applied to Sc $\approx$ 1 and Sc$\gg$1 passive-scalar mixing," Phys. Fluids **20**, 035103 (2008).

[5] D. A. Donzis, K. R. Sreenivasan, and P. K. Yeung, "The Batchelor spectrum for mixing of passive scalars in isotropic turbulence," Flow, Turbul. Combust. **85**, 549 (2010).

[6] S. Komori, T. Kanzaki, Y. Murakami, and H. Ueda, "Simultaneous measurements of instantaneous concentrations of two species being mixed in a turbulent flow by using a combined laser-induced fluorescence and laser-scattering technique," Phys. Fluids A **1**, 349 (1989).

[7] P. L. Miller and P. E. Dimotakis, "Stochastic geometric properties of scalar interfaces in turbulent jets," Phys. Fluids A **3**, 168 (1991).

[8] P. L. Miller and P. E. Dimotakis, "Reynolds number dependence of scalar fluctuations in a high Schmidt number turbulent jet," Phys. Fluids A **3**, 1156 (1991).

[9] P. E. Dimotakis and P. L. Miller, "Some consequences of the boundedness of scalar fluctuations," Phys. Fluids A **2**, 1919 (1990).

[10] T. Gotoh, S. Hatanaka, and H. Miura, "Spectral compact difference hybrid computation of passive scalar in isotropic turbulence," J. Comput. Phys. **231**, 7398 (2012).

[11] T. Ishihara, T. Gotoh, and Y. Kaneda, "Study of high–Reynolds number isotropic turbulence by direct numerical simulation," Annu. Rev. Fluid Mech. **41**, 165 (2009).

[12] I. Calmet and J. Magnaudet, "Large-eddy simulation of high-Schmidt number mass transfer in a turbulent channel flow," Phys. Fluids **9**, 438 (1997).

[13] I. Calmet and J. Magnaudet, "High-Schmidt number mass transfer through turbulent gas-liquid interfaces," Int. J. Heat Fluid Flow **19**, 522 (1998).

[14] J. Magnaudet and I. Calmet, "Turbulent mass transfer through a flat shear-free surface," J. Fluid Mech. **553**, 155 (2006).

[15] G. C. Burton, "Scalar-energy spectra in simulations of Sc$\gg$1 mixing by turbulent jets using the nonlinear large-eddy simulation method," Phys. Fluids **20**, 071701 (2008).

[16] *Implicit Large Eddy Simulation: Computing Turbulent Fluid Dynamics*, edited by F.F.Grinstein, L.G.Margolin, and W.J.Rider (Cambridge University Press, 2007).

[17] O. Desjardins, G. Blanquart, G. Balarac, and H. Pitsch, "High order conservative finite difference scheme for variable density low Mach number turbulent flows," J. Comput. Phys. **227**, 7125 (2008).

[18] S. Orszag, "On the elimination of aliasing in finite-difference schemes by filtering high-wavenumber components," J. Atmos. Sci. **28**, 1074 (1971).

[19] P. K. Yeung, "Multi-scalar triadic interactions in differential diffusion with and without mean scalar gradients," J. Fluid Mech. **321**, 235 (1996).

[20] K. Alvelius, "Random forcing of three-dimensional homogeneous turbulence," Phys. Fluids **11**, 1880 (1999).

[21] R. Nourgaliev and T. Theofanous, "High-fidelity interface tracking in compressible flows: Unlimited anchored adaptive level set," J. Comput. Phys. **224**, 836 (2007).

[22] P. K. Yeung, S. Xu, and K. R. Sreenivasan, "Schmidt number effects on turbulent transport with uniform mean scalar gradient," Phys. Fluids **14**, 4178 (2002).

[23] G. Brethouwer, J. C. R. Hunt, and F. T. M. Nieuwstadt, "Micro-structure and Lagrangian statistics of the scalar field with a mean gradient in isotropic turbulence," J. Fluid Mech. **474**, 193 (2003).